

Type Ia supernova diversity in three-dimensional models[★]

F. K. Röpkel¹, M. Gieseler¹, M. Reinecke¹, C. Travaglio², and W. Hillebrandt¹

¹ Max-Planck-Institut für Astrophysik, Karl-Schwarzschild-Str. 1, 85741 Garching, Germany
e-mail: [fritz; mccg; martin; wfh]@mpa-garching.mpg.de

² INAF - Osservatorio Astronomico di Torino, Strada dell'Osservatorio 20, 10025 Pino Torinese, Torino, Italy
e-mail: travaglio@to.astro.it

Received 13 May 2005 / Accepted 6 January 2006

ABSTRACT

Context. The use of type Ia supernovae as distance indicators for cosmology has initiated a search for theoretical arguments supporting the empirical calibration methods applied. As a first step, a sound understanding of the origin of the observed diversity in type Ia supernova properties is needed.

Aims. Here we present a systematic study of effects resulting from changing some physical parameters of three-dimensional deflagration models of thermonuclear supernovae.

Methods. The high computational costs of such models restricted this survey to simple setups which are known to result in weak explosions and therefore we point out trends rather than setting the absolute scale of the variance. In our study we vary the progenitor's carbon-to-oxygen ratio and its central density prior to ignition because both properties are not well determined by stellar evolution theory and they may change from supernova to supernova. Next we compute for these explosion models the nucleosynthesis yields in a post-processing step. This, in addition, allows us to study variations in the progenitor's metallicity by means of different ²²Ne mass fractions in the initial composition.

Results. We find that the progenitor's carbon-to-oxygen ratio and its central density affect the energy release of the models and thus the expansion velocity of the supernova. Moreover, we find that changing the metallicity and the central density changes the production of radioactive ⁵⁶Ni and thus affects the luminosity. In contrast, the carbon-to-oxygen ratio has little effect on the ⁵⁶Ni production.

Conclusions. Implications of the variations of the explosion energy and the produced ⁵⁶Ni mass for type Ia supernova diversity are discussed.

Key words. stars: supernovae: general – hydrodynamics – nuclear reactions, nucleosynthesis, abundances – methods: numerical

1. Introduction

Type Ia supernovae (SNe Ia) have become a major tool to determine cosmological parameters. As a consequence of their uniformity of properties and their enormous brightness they are suitable for cosmological distance measurements. However, they are not perfect “standard candles”, as they show a significant intrinsic scatter in their peak luminosities as well as other characteristics. Therefore their cosmological application rests on empirical corrections of the peak luminosities based on correlations with other observables (e.g. Phillips 1993). Such empirical corrections facilitated distance measurements of SNe Ia at high redshifts, which have led to the spectacular conclusion that the expansion of the universe is accelerating (Riess et al. 1998; Perlmutter et al. 1999). One way to take this result into account is with a cosmological constant in the Einstein equations possibly indicating a dark energy component of the universe (for a review see Leibundgut 2001).

This underscores the need for a theoretical understanding of the correlation of characteristics that have been established only empirically. A theoretical understanding will help to answer questions such as the possible confounding of calibration procedures with evolutionary effects.

In the astrophysical standard model (see Hillebrandt & Niemeyer 2000), SNe Ia are associated with thermonuclear

explosions of carbon/oxygen white dwarf (WD) stars. The optical event is powered by the decay of radioactive species (e.g. ⁵⁶Ni) produced in thermonuclear burning. Numerical simulations on the basis of this scenario provide an approach to the understanding of calibration methods. Recently, there has been much progress in the three-dimensional modeling of the explosion process (Hillebrandt et al. 2000; Reinecke et al. 2002a,b,c; Gamezo et al. 2003) and the question arises of whether it is possible to reproduce the SN Ia diversity by varying the initial parameters of such models. This will be addressed in the present study where we restrict the survey to so-called deflagration models of thermonuclear supernovae.

After ignition near the center of the WD, the flame propagates outward in the subsonic deflagration mode, i.e. it is mediated by thermal conduction of the degenerate electron gas. This outward burning produces an inverse density stratification in the gravitational field of the WD star with dense fuel on top of hot and light ashes. Consequently, due to buoyancy (Rayleigh-Taylor) instabilities, burning bubbles form that rise into the fuel, leading to shear flows. Kelvin-Helmholtz instabilities generate strong turbulence, given the fact that the typical Reynolds number is of the order of 10¹⁴. The resulting turbulent eddies decay to smaller scales, thereby forming a turbulent energy cascade. The interaction of the thermonuclear flame with these turbulent motions is the key feature of the deflagration model for SNe Ia. A laminar flame would burn far too slowly to release sufficient energy for an explosion of the star. However,

[★] Tables 6 and 7 are only available in electronic form at <http://www.edpsciences.org>

the wrinkling of the flame due to turbulence and the accompanying flame surface enhancement increase the net burning rate and accelerate the flame. This defines the deflagration model of thermonuclear supernova explosions as a problem of turbulent combustion. Reinecke et al. (2002b) and Gamezo et al. (2003) showed that this model indeed leads to an explosion. Whether it reproduces all aspects of observed supernovae is not known (e.g. Kozma et al. 2005). Gamezo et al. (2004) and Höflich et al. (1998) claim that a hypothetical transition from the deflagration mode of flame propagation to a supersonic detonation needs to be invoked at later phases of the explosion. We set aside such a transition because its physical origin is not understood (Niemeyer 1999). Moreover, even in such a case the initial deflagration stage will be essential in understanding SN Ia diversity since large fractions of the energy and the radioactive ^{56}Ni (which powers the lightcurve) are produced here and nonlinear effects in flame propagation are extremely sensitive to the initial conditions.

The crucial role played by three-dimensional effects in deflagration SN Ia models calls for multi-dimensional simulations to study the diversity of such events. Most previous attempts to determine the origin of the SN Ia diversity were, however, based on one-dimensional models (Bravo et al. 1993, 1996; Höflich et al. 1998; Umeda et al. 1999a; Iwamoto et al. 1999; Domínguez & Höflich 2000; Domínguez et al. 2000, 2001). These are hampered by introducing free parameters due to incomplete description of the relevant physics in addition to the initial parameters they intend to study. The description of turbulent mixing as well as the effective flame velocity is not inherent in one-dimensional models but rather is accomplished in a parametrized way. Due to the free parameters, empirical one-dimensional models are not sufficiently predictive to determine explanations for the diversity of SNe Ia, but they can nevertheless provide valuable clues for possible trends. Systematic studies based on three-dimensional models overcome the ambiguity of the turbulent flame velocity and mixing. By correctly modeling these effects, multi-dimensional deflagration models contain no tunable parameters and possess a high predictive power. However, due to the challenging computational demands of three-dimensional models, the available studies of initial parameters are very incomplete.

Applying a simplified setup we present the first systematic survey of the impact of initial parameters on three-dimensional SN Ia models. Due to the simplicity (and possibly incompleteness) of our models we cannot set the absolute scale of the effects in the present parameter study. Nevertheless, we are able to point out the trends of effects of varying the initial parameters.

We restrict this first systematic study to variations of the central density, the initial carbon-to-oxygen (C/O) ratio and the metallicity of the progenitor just prior to ignition. Our intention is to test the parameters independently, setting aside any realistic evolution of the progenitor system. For detailed progenitor evolution studies see e.g. Nomoto & Iben (1985), Hernanz et al. (1988), Bravo et al. (1996), Umeda et al. (1999b), Langer et al. (2000) and Domínguez et al. (2001). Important parameters that are not addressed in this study are for instance rotation and flame ignition (see e.g. Woosley et al. 2004). Some effects of the ignition conditions on SN Ia models and nucleosynthesis have been discussed by Travaglio et al. (2004), Röpke et al. (2006), and Schmidt & Niemeyer (2006).

In Sect. 2 we describe the numerical schemes we apply to model SNe Ia explosions and nucleosynthesis, followed by a discussion of the parameter space to be explored (Sect. 3). The features of the explosion models will be compared in Sect. 5,

and Sect. 6 describes the nucleosynthetic yields of these models. Conclusions are drawn in Sect. 7.

2. Numerical model

The numerical model applied in our study consists of two parts. In a first step we simulate the hydrodynamics of the explosion process. Here, the description of the nuclear processes is very coarse. With the information gained from tracer particles advected in this simulation we perform a nucleosynthetic post-processing as a second step. This enables us to infer the production of the individual isotopes. Both methods will be briefly described in the following.

2.1. Explosion dynamics

The deflagration model of thermonuclear supernova explosions as outlined in Sect. 1 was implemented in a numerical scheme by Reinecke et al. (1999a, 2002a). We refer to these works for the details of the applied techniques and will only mention the basic aspects here.

The major problem of SN Ia simulations is the vast range of relevant scales. The thickness of the flame is tiny compared with the dimensions of the WD star and the turbulent cascade interacts with the flame down to the so-called Gibson scale where the turbulent velocity fluctuations become comparable with the laminar flame speed. Neither the internal flame structure nor the Gibson scale can be resolved in multidimensional simulations in the foreseeable future and thus the flame propagation and turbulence effects have to be adequately modeled in numerical simulations.

Seen from the size of the WD star, it is justified to regard the unresolved flame as a discontinuity separating the fuel from the ashes. The description of flame propagation then has to track this interface and a technique well-suited for this purpose is the so-called *level set method* (Osher & Sethian 1988). It is widely used in simulations of combustion problems in engineering. In this technique, the flame front is associated with the zero level set of a scalar field G . For numerical reasons, G is chosen to be a signed distance function with respect to the flame front. To model the flame propagation we evolve the G -field according to the scheme described by Reinecke et al. (1999b).

In this scheme the effective flame velocity has to be provided. It is essential that turbulent combustion proceeds in different regimes (e.g. Peters 2000). For most parts of the supernova explosion the so-called *flamelet regime* applies, where the flame as a whole is wrinkled by turbulence. Here, the flame propagation is known to decouple from the microphysics of the burning process and to be determined by the turbulent motions exclusively (Damköhler 1940). These, however, are derived from a *subgrid-scale model* implemented first in SN Ia simulations by Niemeyer & Hillebrandt (1995). It describes the effects of turbulence on unresolved scales. In this sense our model can be regarded as a Large Eddy Simulation (LES) well-known from computational fluid dynamics. Since flame propagation is modeled in our simulations, supplementary simulations of the physical processes on small scales have to be provided that ensure the validity of the underlying assumptions. For instance, Röpke et al. (2003, 2004a,b) showed that flame propagation proceeds in a stabilized way below the Gibson scale.

The hydrodynamics is modeled based on the PROMETHEUS implementation (Fryxell et al. 1989) of the piecewise parabolic method (Colella & Woodward 1984).

The equation of state of the WD material comprises contributions from a variably degenerate and relativistic electron gas, ions following the Boltzmann statistics, a photon gas and electron/positron pairs.

The most correct way to incorporate the nuclear burning would require a full reaction network. However, due to the restricted computational resources only a very simplified description of the nucleosynthesis is possible in the explosion simulation. Our implementation follows the approach suggested by Reinecke et al. (2002a), who include five species, viz. α -particles, ^{12}C , ^{16}O , “Mg” as a representative of intermediate mass elements and “Ni” representing iron group nuclei¹. The fuel is assumed to be a mixture of carbon and oxygen. At the initial high densities, burning proceeds to nuclear statistical equilibrium (NSE) composed of α -particles and “Ni”. Depending on temperature and density in the ashes, the NSE composition changes, which has a significant impact on the explosion dynamics (Reinecke et al. 2002a). Once the fuel density drops below $5.25 \times 10^7 \text{ g cm}^{-3}$ due to the expansion of the WD, burning is assumed to terminate at intermediate mass elements. Below $1 \times 10^7 \text{ g cm}^{-3}$ burning is switched off, since it is then expected to leave the flamelet regime and to enter the so-called distributed burning regime. Here turbulence penetrates the internal structure of the flame. This effect is ignored in the present study but was addressed by Röpke & Hillebrandt (2005b).

In order to achieve a more detailed analysis of the nucleosynthetic yields of the simulated supernova explosion we advect tracer particles with the fluid motions recording temperature, density and internal energy as a function of time. These data then serve as input for a nucleosynthetic postprocessing.

2.2. Nuclear postprocessing

The nuclear postprocessing determines the nucleosynthetic yields of the explosion models a posteriori from the data recorded by the tracer particles. The applied method is similar to that described by Thielemann et al. (1986) (there labeled as *method (a) simple postprocessing*). Its application to SNe Ia explosions is discussed in detail by Travaglio et al. (2004).

The employed nuclear reaction network code was kindly provided by Thielemann. It comprises 384 isotopes which are listed in Table 1 and takes into account β -decays, electron captures, photo-disintegrations, two-body reactions and three-body reactions. A detailed description of the network is given by Thielemann et al. (1996) and Iwamoto et al. (1999). As Brachwitz et al. (2000) and Thielemann et al. (2003) discussed previously, the new electron capture and β -decay rates by Langanke & Martínez-Pinedo (2000) and Martínez-Pinedo et al. (2000) are included in the network.

Since the description of the nuclear reactions in the hydrodynamic explosion simulation is coarse and Y_e is assumed to be constant at a value of 0.5, the internal energy recorded by the tracer particles is employed to calculate a realistic temperature from a high-temperature equation of state (Timmes & Swesty 2000) combined with an improved nuclear reaction network (cf. Travaglio et al. 2004).

The nucleosynthesis is calculated separately for each tracer particle. To smooth variations in the data from the hydrodynamic simulation, the minimal temperature is set to 10^9 K . This

¹ In the following we set “Ni” and “Mg” in quotes when we refer to the iron group elements and intermediate mass elements followed in the explosion hydro-simulations. This is done to avoid confusion with the results of the nuclear postprocessing.

Table 1. Nuclear reaction network (note that the elements below arsenic are irrelevant for SNe Ia).

Element	Atomic mass A	Element	Atomic mass A
n	1	Sc	40 ... 50
p	1	Ti	42 ... 52
He	4, 6	V	44 ... 54
Li	6, 7, 8	Cr	46 ... 56
Be	7, 9, 10, 11	Mn	48 ... 58
B	8, 9 ... 12	Fe	50 ... 62
C	10 ... 15	Co	52 ... 63
N	12 ... 17	Ni	54 ... 67
O	14 ... 20	Cu	56 ... 69
F	17 ... 21	Zn	59 ... 72
Ne	18 ... 25	Ga	61 ... 76
Na	20 ... 26	Ge	63 ... 78
Mg	21 ... 28	As	71 ... 80
Al	23 ... 30	Se	74 ... 83
Si	25 ... 33	Br	75 ... 83
P	27 ... 35	Kr	78 ... 87
S	29 ... 38	Rb	79 ... 87
Cl	31 ... 40	Sr	84 ... 91
Ar	33 ... 44	Y	85 ... 91
K	35 ... 46	Nb	91 ... 97
Ca	37 ... 49	Mo	92 ... 98

measure guarantees stability of the nuclear reaction network code. Subsequently, the maximum temperature T_{max} is checked. If it does not exceed $2 \times 10^9 \text{ K}$, then the corresponding material is treated as unprocessed. This approach is justified since the fuel consists only of ^{12}C , ^{16}O and ^{22}Ne , which below $2 \times 10^9 \text{ K}$ will burn hydrostatically, not contributing significantly to the nucleosynthetic yields over the simulated period of time.

For tracers with $T_{\text{max}} > 2 \times 10^9 \text{ K}$ the following procedure is applied:

1. Nuclear statistical equilibrium (NSE) is assumed if the temperature of the current time step t_i is larger than $6 \times 10^9 \text{ K}$, i.e. the strong reactions can be neglected and only the “weak” nuclear network is applied updating Y_e . Otherwise the full reaction network is employed.
2. Temperature and density are interpolated for the sample point at t_{i+1} . If these variables change for more than 5% in the interval $[t_i, t_{i+1}]$, the time step is halved.
3. The network is solved for t_{i+1} . If a relative accuracy of 10^{-5} cannot be reached in a limited number of steps, the time step is again halved and we resume with point 2 of the scheme. If this measure fails, the tracer is ignored in the final result. Fortunately the number of such cases could be drastically reduced to at most one out of $[27]^3$. When reaching NSE the new abundances are calculated for the updated Y_e at t_{i+1} .
4. If the abundance of an isotope drops below 10^{-25} , it is set to zero.

3. Parameter space

The initial parameters we explore in our study (the carbon mass fraction $X(^{12}\text{C})$, the central density ρ_c and the metallicity Z of the WD at ignition) are treated as independent. This allows us to disentangle the effects of the individual parameters on the explosion process. Nonetheless, the parameter space is chosen in agreement with values suggested by stellar evolution, as described below.

Different values for the central density of the WD and the carbon-to-oxygen ratio of its material are applied in the

Table 2. Model parameters.

Model	ρ_c [10^9 g cm^{-3}]	$X(^{12}\text{C})$	Metallicity
<i>1_1_1</i>	1.0	0.30	$0.5 Z_\odot$
<i>1_1_2</i>	1.0	0.30	$1.0 Z_\odot$
<i>1_1_3</i>	1.0	0.30	$3.0 Z_\odot$
<i>1_2_1</i>	1.0	0.46	$0.5 Z_\odot$
<i>1_2_2</i>	1.0	0.46	$1.0 Z_\odot$
<i>1_2_3</i>	1.0	0.46	$3.0 Z_\odot$
<i>1_3_1</i>	1.0	0.62	$0.5 Z_\odot$
<i>1_3_2</i>	1.0	0.62	$1.0 Z_\odot$
<i>1_3_3</i>	1.0	0.62	$3.0 Z_\odot$
<i>2_1_1</i>	2.6	0.30	$0.5 Z_\odot$
<i>2_1_2</i>	2.6	0.30	$1.0 Z_\odot$
<i>2_1_3</i>	2.6	0.30	$3.0 Z_\odot$
<i>2_2_1</i>	2.6	0.46	$0.5 Z_\odot$
<i>2_2_2</i>	2.6	0.46	$1.0 Z_\odot$
<i>2_2_3</i>	2.6	0.46	$3.0 Z_\odot$
<i>2_3_1</i>	2.6	0.62	$0.5 Z_\odot$
<i>2_3_2</i>	2.6	0.62	$1.0 Z_\odot$
<i>2_3_3</i>	2.6	0.62	$3.0 Z_\odot$

explosion model itself. Contrary to that, we vary the metallicity only in the nucleosynthesis postprocessing. The nomenclature of the models is given in Table 2.

3.1. Variation of the carbon mass fraction

The origin of the diversity in the carbon mass fraction has been studied by Umeda et al. (1999b) by numerically evolving the corresponding binary systems with 3–9 M_\odot WD progenitor stars. They found it to depend on the metallicity and the zero-age main sequence (ZAMS) mass of the WD progenitor, as well as on the mass of the companion star. These in turn determine the mass of the WD, $M_{\text{WD},0}$, just prior to the onset of accretion. The main outcome of the survey was that $X(^{12}\text{C})$ in the core of the WD decreases with increasing $M_{\text{WD},0}$ and that the direct dependence of $X(^{12}\text{C})$ on the metallicity is small although the correlation between the ZAMS mass and $M_{\text{WD},0}$ depends sensitively on it (Umeda et al. 1999a). Taking into account the conditions ensuring that the WD will accrete mass until reaching M_{Ch} , Umeda et al. (1999b) infer that $X(^{12}\text{C})$ may vary in the range from ~ 0.36 to ~ 0.5 . These values apply only to the convective core of the WD. The accreted material is assumed to be processed to a C/O ratio of ~ 1 , leading to a gradient of the carbon mass fraction inside the WD. This effect will be ignored in our model, where we postulate a uniform C/O ratio throughout the entire star employing values of 0.30, 0.46 and 0.62 for $X(^{12}\text{C})$ (cf. Table 2).

3.2. Variation of the central density

The variation of the central density in SN Ia progenitors just before the ignition of the flame is even more difficult to constrain. At least two effects determine the value of ρ_c .

The first is the accretion history of the binary system (see Langer et al. 2000, for a detailed study of the accretion process). There seems to be only a narrow window in the range of possible accretion rates \dot{M} in which carbon can be ignited centrally, avoiding off-center ignitions and gravitational collapse due to high electron-capture rates. Nomoto & Iben (1985) report two centrally ignited models with $\rho_c = 1.7 \times 10^9 \text{ g cm}^{-3}$ and $\rho_c = 5.2 \times 10^9 \text{ g cm}^{-3}$, respectively, and Bravo et al. (1996) find

models in the range $1.8 \times 10^9 \text{ g cm}^{-3} \lesssim \rho_c \lesssim 6.3 \times 10^9 \text{ g cm}^{-3}$. However, the exact range of that window is uncertain and depends additionally on the white dwarf mass and temperature. Initially cooler WDs are shifted to rather high central densities in the range $6 \times 10^9 \text{ g cm}^{-3} \lesssim \rho_c \lesssim 1.3 \times 10^{10} \text{ g cm}^{-3}$ (Hernanz et al. 1988).

The second effect is the establishment of the thermal structure of the WD. Cooling due to plasmon neutrino losses and neutrino bremsstrahlung have to be taken into account (Iwamoto et al. 1999), and a (most uncertain) contribution may come from the convective Urca process (Paczynski 1972; Barkat & Wheeler 1990; Mochkovitch 1996; Lesaffre et al. 2005).

Bravo et al. (1993) calculate models for central densities of $2.5 \times 10^9 \text{ g cm}^{-3}$, $4.0 \times 10^9 \text{ g cm}^{-3}$ and $8.0 \times 10^9 \text{ g cm}^{-3}$ at ignition, and Iwamoto et al. (1999) use values of $1.37 \times 10^9 \text{ g cm}^{-3}$ and $2.12 \times 10^9 \text{ g cm}^{-3}$. We assume central densities of $1.0 \times 10^9 \text{ g cm}^{-3}$ and $2.6 \times 10^9 \text{ g cm}^{-3}$ (see Table 2). Unfortunately it is not yet possible to apply higher central densities, since then electron captures will become dynamically important. Although electron captures are correctly treated in the nuclear postprocessing, this effect is not implemented in the current explosion models.

3.3. Variation of the metallicity

Our ignorance concerning realistic progenitor evolution is evident in the approach to prescribe the metallicity Z of the progenitor independent of the other parameters. Detailed stellar evolution calculations (e.g. Umeda et al. 1999b; Domínguez et al. 2001) have shown that it strongly influences the progenitor's central density and also the C/O ratio. Nevertheless, in the spirit of our exploration of possible effects in the explosion models, we set aside a realistic progenitor description and treat the metallicity as an independent parameter. A direct effect of the metallicity of the WD's progenitor is the ^{14}N abundance after the CNO burning phase. During helium burning it is then converted mostly to ^{22}Ne . For simplicity, we assume a uniform distribution of this ^{22}Ne , which is only justified in regions mixed by pre-ignition convection.

An analytic estimation of the effect of the metallicity on the ^{56}Ni production was given by Timmes et al. (2003). They suggest a variation of Z ranging from 1/3 to 3 times solar, based on observations of field white dwarfs. Following this suggestion we vary the ^{22}Ne abundance in our models to simulate a variation in metallicity Z . In particular we explore Z_\odot (corresponding to $X(^{22}\text{Ne}) = 0.025$), $0.5 Z_\odot$ and $3 Z_\odot$ (cf. Table 2).

4. Simulation setup

Several simulations are necessary to cover the required parameter space. We therefore have to minimize the computational expenses by applying a simple setup for the individual models. Our calculations span only one spatial octant and assume mirror symmetry to the other octants. Full-star simulations (Röpke & Hillebrandt 2005a) have shown that this approach does not miss large-scale flame features and thus – although a simplification – does not restrict the validity of the model. The simulations were set up on a Cartesian computational grid that was equally spaced in the inner regions. To capture the expansion of the WD, the outer grid cells were widened exponentially. Recently, Röpke (2005) showed that with a comoving computational grid the evolution can be followed to homologous expansion. This, however, is not applied in the present models.

The resolution of the individual runs was rather low – the computational domain was divided in $[256]^3$ grid cells

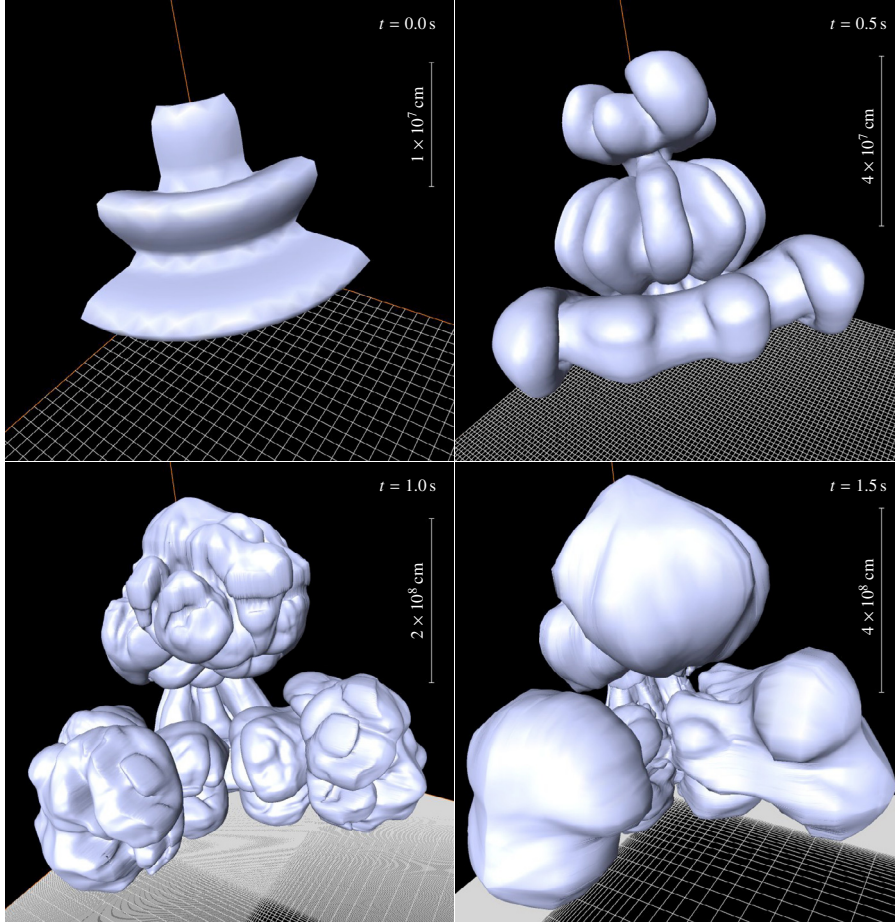


Fig. 1. Time evolution of the burning front for model 2_2_X.

corresponding to a central grid resolution of 10^6 cm. In each direction the grid length in the outer 35 zones was increased subsequently by a factor of 1.15. As was pointed out by Reinecke et al. (2002c) the chosen resolution still guarantees numerical convergence in the explosion characteristics (possibly with the exception of the latest stages of the burning where intermediate mass elements are produced). This convergence was demonstrated there only for two-dimensional simulations. However, since the convergence is not a result of resolving turbulence effects on all relevant scales (which will never be possible) but rather results from an interplay of the resolved scales with the subgrid-scale turbulence model, it is justified to assume a similar behavior in three-dimensional models.

With the chosen resolution it is not possible to set up reasonable multi-point ignition scenarios, as only a very small number of seed-bubbles could be resolved. This is a drawback because Reinecke et al. (2002b) showed that such models give rise to more vigorous explosions. We restrict our simulations to the centrally ignited *c3_3d_256* model of Reinecke et al. (2002c) in which the spherical initial flame geometry is perturbed with three toroidal rings (see the upper left panel of Fig. 1). Note that we initially incinerate the same volume in all models, which does not correspond to the same mass for different central densities. This ensures the same initial numerical resolution of the flame front.

For the construction of a WD near the Chandrasekhar mass we follow the procedure described by Reinecke (2001). We assume a cold isothermal WD of a temperature $T_0 = 5 \times 10^5$ K. With the chosen values for the carbon mass fraction of the

material and the central density we integrate the equations of hydrostatic equilibrium using the equation of state described in Sect. 2.1. Depending on the central densities and compositions, the masses of the resulting WDs vary slightly: for $\rho_c = 1.0 \times 10^9$ g cm $^{-3}$ and $\rho_c = 2.6 \times 10^9$ g cm $^{-3}$ the WD masses amount to $1.367 M_\odot$ and $1.403 M_\odot$, respectively. As tested by Reinecke (2001), the construction procedure guarantees stability of the WD over a time longer than simulated.

The $[n_{\text{trace}}]^3$ tracer particles are distributed in an $n_{\text{trace}} \times n_{\text{trace}} \times n_{\text{trace}}$ equidistant grid in the integrated mass $M_0(r)$, the azimuthal angle ϕ , and $\cos\theta$, so that each particle represents the same amount of mass. In order to improve the tracer particle statistics, a random offset to the coordinates was applied. This offset was chosen small enough to keep the tracer particles in their individual mass cells. The values of the density, the temperature and the internal energy at the tracer particle's location and its coordinates were recorded every ~ 1 ms. This allows for an accurate reconstruction of the trajectories as well as the final velocities and the thermodynamical data. In the models presented in the following we set $n_{\text{trace}} = 27$. To test the representation of the model in the tracer particles in cases of low central densities, this number was increased to 35 in test calculations, as will be discussed below.

5. Explosion models

The explosion simulation for model 2_2_X (the metallicity does not affect the explosion dynamics in our implementation) at four different times is illustrated in Fig. 1. The isosurface indicating

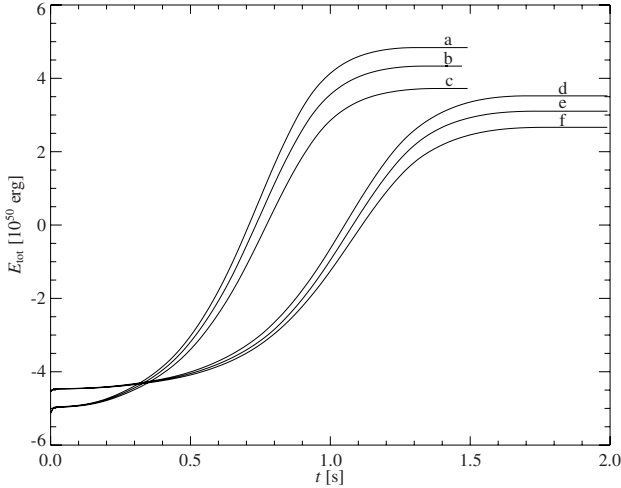


Fig. 2. Total energies in models **a)** 2_3_X, **b)** 2_2_X, **c)** 2_1_X, **d)** 1_3_X, **e)** 1_2_X and **f)** 1_1_X.

Table 3. Results of explosion models: produced masses of iron group elements (“Ni”) and intermediate mass elements (“Mg”), nuclear energy release and total energy at the end of the simulations.

Model	$M(“\text{Ni}”)$ [M_{\odot}]	$M(“\text{Mg}”)$ [M_{\odot}]	E_{nuc} [10^{50} erg]	E_{tot} [10^{50} erg]
1_1_X	0.3944	0.2067	6.974	2.714
1_2_X	0.3867	0.2081	7.445	3.140
1_3_X	0.3757	0.2144	7.870	3.563
2_1_X	0.5178	0.1874	8.851	3.772
2_2_X	0.5165	0.1859	9.461	4.412
2_3_X	0.5104	0.1822	9.966	4.909

the position of the flame front is determined from the zero level set of the scalar field G . The computational grid plotted in these snapshots shows our setup with uniform grid cells in the inner region and an exponential growth of the grid spacing further out. Our initial flame configuration is shown in the upper left snapshot of Fig. 1. In the subsequent snapshots the growth of instabilities and an increasing wrinkling of the flame front are visible. Once the flame enters the exponentially growing part of the grid, the resolution of flame features becomes coarser. However, at this stage the expansion of the WD decreases the density of the fuel to values where burning has largely ceased in our model. Thus the coarse flame resolution in late stages of the simulation does not affect the results.

Figure 2 shows the total energy production of our models. Due to the simple setup, all explosions are weak, but trends can clearly be identified. The energy releases of the different models are listed in Table 3, which also provides the masses of produced iron group elements (“Ni”) and intermediate mass elements (“Mg”). In Figs. 3 and 4 the energy generation rates and the evolution of the turbulent energies in our models are plotted.

5.1. Variation of the progenitor’s C/O ratio

The effects of a variation of the progenitor’s carbon-to-oxygen ratio on the SN Ia explosion models have been described by Röpke & Hillebrandt (2004). We extend the discussion here.

Considering the explosion energetics first, Fig. 2 shows that a higher carbon mass fraction leads to an increased energy production for fixed central densities. Values are given in Table 3. Changing $X(^{12}\text{C})$ from 0.30 to 0.62 the nuclear energy releases

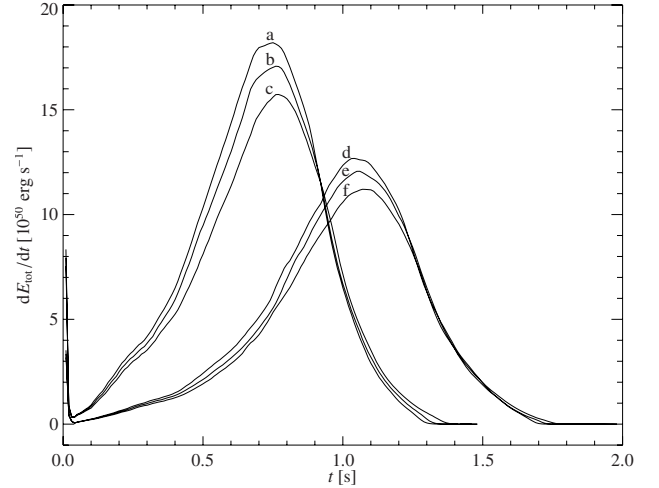


Fig. 3. Energy generation rates in models **a)** 2_3_X, **b)** 2_2_X, **c)** 2_1_X, **d)** 1_3_X, **e)** 1_2_X and **f)** 1_1_X.

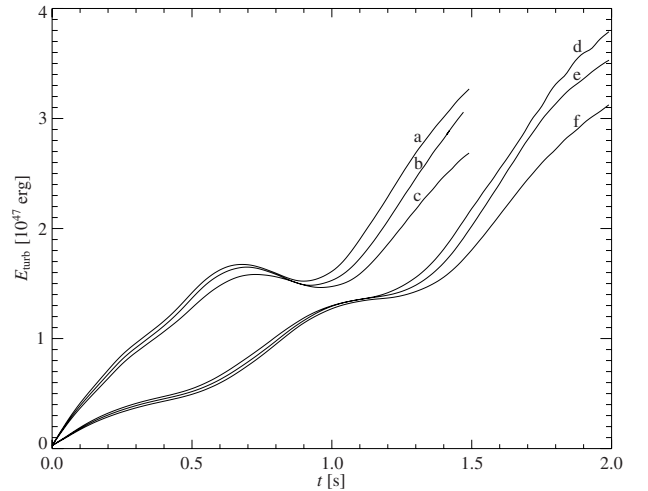


Fig. 4. Turbulent energies in models **a)** 2_3_X, **b)** 2_2_X, **c)** 2_1_X, **d)** 1_3_X, **e)** 1_2_X and **f)** 1_1_X.

of the models increase by 12% ($\sim 27\%$ in the total energies) for both central densities. The observed trend is not surprising and can easily be explained by the burning process. The predominant effect is the difference in the mean binding energy of the fuel. A higher carbon mass fraction increases the total energy generation simply because the binding energy of ^{12}C is lower than that of ^{16}O so that it releases more energy by fusion to iron group elements. A minor effect could be that the laminar burning velocity increases with $X(^{12}\text{C})$ (Timmes & Woosley 1992). This, however, is negligible in our models, since already after a few time steps the flame propagation is completely determined by the turbulent flame speed.

The evolution of the energetics in the models does not show a strong temporal shift. The energy generation rate peaks at comparable times for the models with different carbon mass fractions (cf. Fig. 3 for the temporal evolution of the energy generation rate²). Figure 2 reveals that the total energies of our models are very similar for the largest part of the energy generation and differ only in the late phases. In this point our findings disagree with Khokhlov (2000). Although he speculates that a decreasing

² Note that the peak at $t = 0$ s is caused by our setup in which the initial flame is initialized by instantly incinerating the material behind it.

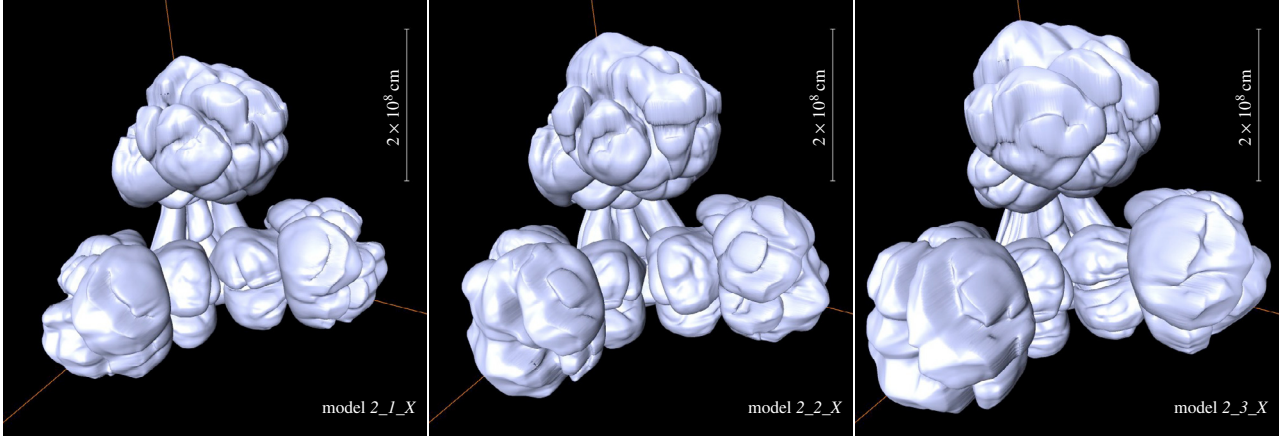


Fig. 5. Flame surface of models with different carbon mass fraction at $t = 1.0$ s.

$X(^{12}\text{C})$ would result in weaker explosions, he claims that the reason is a delay of the development of the buoyancy instabilities, which seems to be only a minor effect in our simulations. The reason for the difference in the interpretation of the results is possibly that the models of Khokhlov (2000) were apparently not evolved beyond the maximum of energy generation so that it is difficult to distinguish between a delay and an overall lower energy production.

Contrary to the explosion energetics, the produced masses of iron group elements are unexpected. The working hypothesis by Umeda et al. (1999a) predicting a larger production of ^{56}Ni for larger carbon mass fractions was based on the speculation that the resulting increased energy release would enhance buoyancy effects and thus accelerate the turbulent flame propagation. Consequently, more material would be burnt at high velocities producing larger fractions of iron group elements. As emphasized by Umeda et al. (1999a), this hypothesis can only be tested in multi-dimensional simulations that treat the turbulent flame velocity in an unparametrized way. This is provided by our approach, but surprisingly our models do not support the hypothesis. The energies in our models evolve similarly in the first part of the explosion and no enhanced turbulent flame propagation is visible regardless of the carbon mass fraction. The similar temporal evolution of the energetics in our models corresponds to a striking similarity in the flame morphology. Figure 5 illustrates the flame front in models with different C/O ratios at $t = 1.0$ s. The extent of the burnt volumes is comparable. The similarities in the first part of the energy generation as well as in the flame morphologies and flame propagations indicate that the large scale buoyancy effects, which feed energy into the turbulent cascade and thereby drive the flame propagation, are comparable in models with different C/O ratios. The buoyant velocities can be estimated from the relation

$$v_{\text{buoy}} \sim \sqrt{gAtL} \quad (1)$$

for a single non-burning rising bubble of size L subject to a gravitational acceleration g (Davies & Taylor 1950). The Atwood number At characterizes the contrast between the density inside the bubble (ρ_i) and outside it (ρ_o):

$$At = \frac{|\rho_o - \rho_i|}{\rho_o + \rho_i}. \quad (2)$$

In a supernova explosion, the situation is, of course, much more complex since bubbles burn and will merge. Nevertheless,

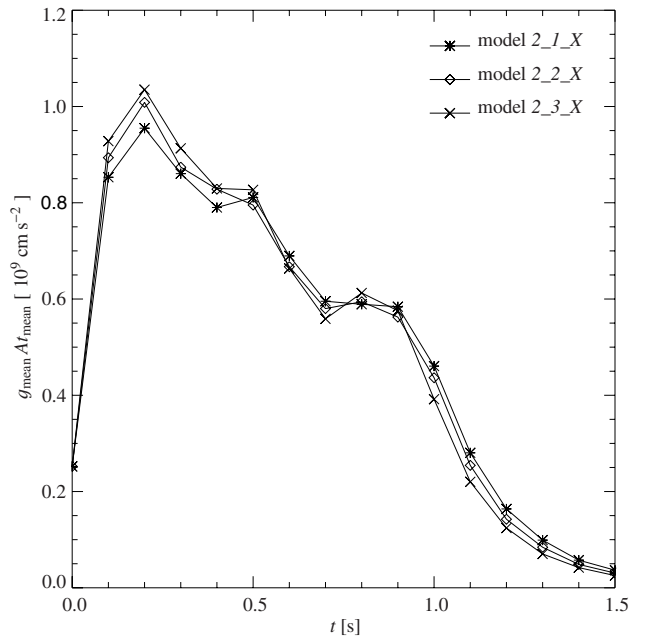


Fig. 6. Mean effective gravitational accelerations experienced by the flame fronts for models with different C/O ratios.

it is clear that the effective gravitational acceleration (gAt) determines the flame propagation velocity – not only directly on the largest scales but also over the mechanism of the interaction of the flame with generated turbulence. This effect can only be revealed in multidimensional calculations, as presented here. Figure 6 shows the mean effective gravitational acceleration experienced by the flame front. Only minor differences are visible. The data point at $t = 0.0$ s is unphysical, since the material behind the flame had not been burnt at this instant and thus there is no density contrast over the flame yet. With temporal evolution there is a competition between a rapidly decreasing gravitational acceleration due to the expansion of the star in the explosion and an increasing density contrast over the flame along with lower fuel densities (cf. Timmes & Woosley 1992). As seen from Fig. 6, the decreasing gravitational acceleration finally dominates this competition.

Because of the very similar evolution of the large-scale buoyancy effects, there are few differences in the evolution of the

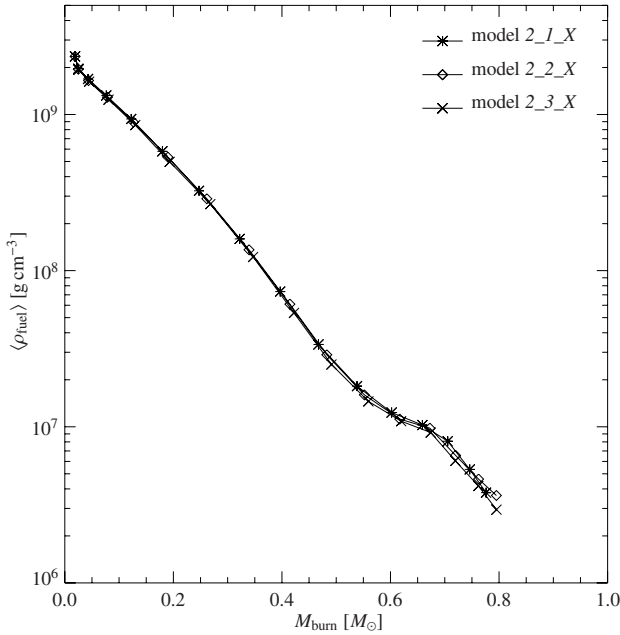


Fig. 7. Fuel densities at the mean flame locations as a function of the mass of “ashes” behind the flame front for models with different carbon mass fraction of the progenitor material.

turbulent energies in models with varying carbon mass fractions (see Fig. 4³).

If the larger energy from burning carbon-rich fuel was directly converted to work expanding the ashes, buoyancy effects and an acceleration of the turbulent flame propagation should be observable in our simulations. The only way to bypass these effects is that the energy is buffered in a larger fraction of α -particles present in the NSE. This fraction indeed increases with higher temperatures and the consequences are twofold. First, the binding energy of the ashes is lowered and less energy is released from thermonuclear burning. Second, distributing the energy over an increased number of particles in the ashes decreases their temperature. Both effects lead to an increase in the density of the ashes which suppresses the buoyancy effects. Hence the turbulent flame propagation velocity in carbon-rich fuel models is lowered to values comparable to those found in oxygen-rich fuel simulations. As a consequence similar masses of fuel are burnt at particular fuel densities. To corroborate this, we plot the fuel density at the average flame front location over the burnt mass in Fig. 7.

Figure 8 proves that the effect of energy buffering in the α -particles indeed applies for our models, here shown for the models with a central density of 2.6 g cm^{-3} . Between 0.2 s and 0.9 s the ashes contain significant amounts of α -particles. The maximum mass fraction of α -particles increases by about 20% when changing the carbon mass fraction from 0.30 to 0.62. This effect is capable of compensating the differences in the fuel binding energies according to the following estimate. At $t \sim 0.6$ s (the energy generation rate peaks here, cf. Fig. 3) the ashes in the model 2_2_X contain about 21% α -particles and 79% “Ni”.

³ The values of E_{turb} are not significant at late times since those are derived from the subgrid energy which depends on the length of the grid cells. In the outer regions which the flame enters at late times, those are elongated and therefore E_{turb} rises again after reaching a peak at $t \sim 0.65$ s and $t \sim 1.05$ s for $\rho_c = 2.6 \times 10^9 \text{ g cm}^{-3}$ and $\rho_c = 1.0 \times 10^9 \text{ g cm}^{-3}$, respectively. For a uniform grid it would be expected to monotonically decrease after these peaks (cf. Röpke 2005).

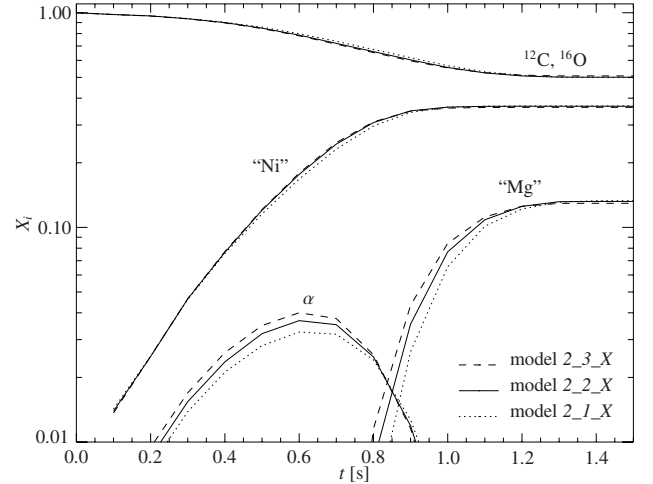


Fig. 8. Temporal evolution of the chemical composition in models with different carbon mass fraction of the progenitor material.

If there was no change in the abundance of α -particles along with changing the C/O ratio in the models, the nuclear energy release would increase by about 22%, changing $X(^{12}\text{C})$ from 0.30 to 0.62. In contrast, taking into account the observed 20% increase in the α -particles in the ashes, the nuclear energy release difference reduces to $\sim 5\%$.

This self-regulation mechanism has an important consequence. Since it suppresses increased buoyancy effects which would otherwise arise with larger carbon mass fractions in the fuel, similar amounts of fuel are consumed by the flame at stages where burning terminates in NSE. Therefore the amount of produced iron group elements is nearly kept constant for different C/O ratios in the fuel.

The α -particles buffer the energy only temporarily. With further expansion and cooling of the WD they are converted to iron group elements (“Ni”) releasing the stored energy. This is the reason why the energies in the models diverge at later times. Then, however, the fuel density has dropped to values where burning terminates in intermediate mass elements and hence the synthesis of iron group elements is unaffected. Therefore the models with different carbon-to-oxygen ratios produce similar amounts of iron group elements. Interestingly, we find even a slight decrease in the production of iron group elements for an increasing carbon mass fraction of the model. The same holds for the intermediate mass nuclei in the high central density models while the trend is reversed in the models with lower central densities (cf. Table 3).

5.2. Variation of the central density

For higher central densities at ignition, the explosion is more vigorous for a fixed carbon mass fraction in the WD material (cf. Fig. 2, Table 3). Here, the nuclear energy release differs by about 26% and the total energies vary by about 34%.

As for an increased carbon mass fraction, a higher density of the fuel accelerates the laminar burning (Timmes & Woosley 1992). Again, this has little impact on our models since burning proceeds in a laminar flame only in the first few time steps. Two other effects are more significant here.

First, for the higher central density, obviously more material is present that can potentially be burnt to iron group elements.

Second, for higher central densities the effective gravitational acceleration experienced by the flame is higher in the

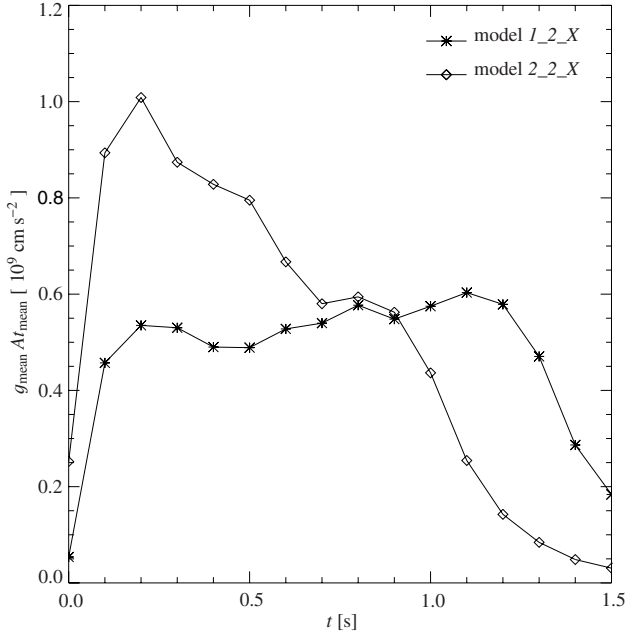


Fig. 9. Mean effective gravitational accelerations experienced by the flame fronts for models with different central densities.

first ~ 0.9 s (cf. Fig. 9). This increases the development of flame structures resulting from the non-linear stage of the buoyancy instability. As a result, the turbulent cascade will develop more quickly (cf. Fig. 4) and the turbulence-induced boost of the effective flame propagation velocity sets in earlier. This is shown in Fig. 10, where snapshots of the flame evolution at fixed times for models with different central densities at ignition are given.

Consequently, the production of iron group elements increases with higher central densities, while the amount of intermediate mass elements decreases.

6. Nucleosynthesis

After the nucleosynthesis postprocessing the abundances of the individual isotopes in the ashes are revealed. Additionally, the parameter of the progenitor’s metallicity comes into play here by assuming a certain fraction of the material to be composed of ^{22}Ne .

The optical event of SNe Ia is powered by the radioactive decay of ^{56}Ni and ^{56}Co . Therefore their peak luminosities are determined by the nucleosynthetic yields of the explosions rather than the energetics. Consequently, the nucleosynthetic postprocessing of explosion models can shed some light on the observed diversity of SN Ia events. ^{56}Co decay is slow and thus the peak luminosity is a function of the produced amount of ^{56}Ni . A compilation of the ^{56}Ni masses derived from all our models by nucleosynthetic postprocessing can be found in Table 4.

Although we will focus here on the effect of initial parameters on the production of ^{56}Ni , we will first discuss the overall nucleosynthesis yields.

6.1. The final yields

The freeze-out masses after completion of the β -decays are plotted in Figs. 11 to 13 for different models. Here the usual normalization to the solar abundances and the ^{56}Fe mass fraction was applied. Values are given in Table 6 in the online material.

Figure 11 shows a comparison between models with different carbon mass fractions for fixed $\rho_c = 2.6 \times 10^9 \text{ g cm}^{-3}$ and for solar metallicity. Obviously, the carbon mass fraction has only little effect on the final abundances. Though some variation is visible for the intermediate mass elements (Mg to Ca), there is practically no difference in the iron group yields for the different models. This is expected from the analysis of the explosion process in the previous section. Due to the energy buffering in the α -particles, burning to NSE consumes almost identical masses of fuel, while the recombination of the α -particles at the end of complete NSE burning leads to an additional energy release that varies with the C/O ratio. Therefore the incomplete burning in the models that follows burning to NSE proceeds differently in the various models.

The variations in the final yields due to different central densities are illustrated in Fig. 12. Here, the models X_2_2 are plotted, i.e. the C/O ratio is fixed to 0.81 and the metallicity is solar. The model with lower central density produces more intermediate mass elements, but the variations are small. In contrast, for higher central densities, there is a visible increase in the abundances of iron group isotopes, viz. titanium, vanadium, chromium, manganese, iron, cobalt and nickel. The two effects that contribute to an increased mass consumption in complete NSE burning with higher ρ_c were discussed in Sect. 5.2. The resulting final yields are a natural consequence of these effects.

Changes in the progenitor’s metallicity resulting in different abundances of ^{22}Ne in the WD material have a large impact on the final yields. To illustrate this influence, we consider the models 2_2_X for $0.5 Z_\odot$, $1.0 Z_\odot$ and $3.0 Z_\odot$ (cf. Fig. 13). The variation of the ^{22}Ne abundance is obvious and caused by the representation of the progenitor’s metallicity in the different mass fractions of that isotope in our simulations. The production of chromium, manganese and iron isotopes is increased for higher metallicity, especially for isotopes with two more neutrons than the symmetric nuclei (^{54}Fe , ^{58}Ni). An exception is ^{56}Fe which was used to normalize the abundances. This trend holds analogously for intermediate mass elements. In particular, one observes a higher abundance of ^{26}Mg , ^{30}Si , ^{34}S , ^{38}Ar and ^{42}Ca with increased metallicity. Comparing the models 2_2_2 and 2_2_3 the change is by a factor of 11 for ^{26}Mg and a factor of approximately 3 for the other isotopes (cf. Table 6 in the online material). The other models not present in the table give similar factors for identical metallicities. The increase of neutron-rich isotopes is caused by the fact that a higher progenitor’s metallicity results in an increased ^{22}Ne mass fraction, which serves as a source of a neutron excess.

6.2. Impact of the C/O ratio on the ^{56}Ni mass

Contrary to the previous section, we analyze here the nucleosynthesis yields immediately after the explosion. The production of radioactive species is given in Table 7 in the online material.

Figure 14 shows the ^{56}Ni production for the models as a function of the carbon mass fraction of the progenitor. The central densities are fixed to $\rho_c = 1.0 \times 10^9 \text{ g cm}^{-3}$ and $\rho_c = 2.6 \times 10^9 \text{ g cm}^{-3}$, respectively. The metallicities of the models shown here are set to $Z = Z_\odot$. We note only minor changes in the ^{56}Ni masses (about 2%) for both central densities, which is not surprising given the small variations in the flame morphology and advancement discussed in Sect. 5.2.

In Fig. 14 the trend of ^{56}Ni production has opposite directions for different central densities. While this feature is in accordance with the total production of iron group elements in the explosion models for low central densities, it is reversed for the

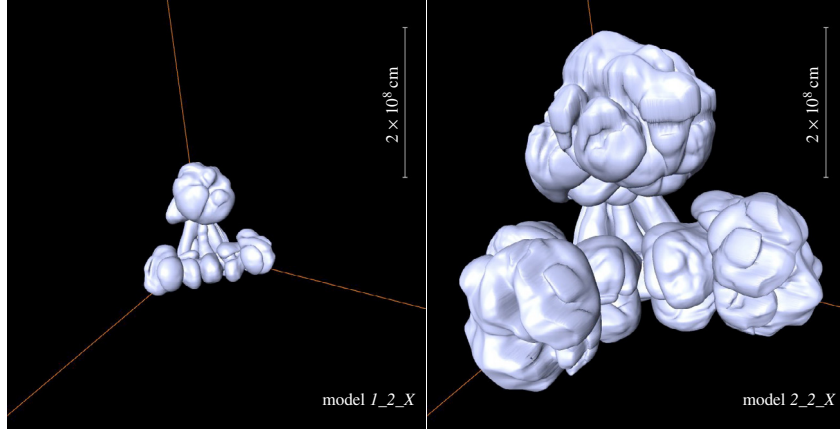


Fig. 10. Flame surface of models with different central densities prior to ignition at $t = 1.0$ s.

Table 4. ^{56}Ni masses synthesized according to the nucleosynthesis postprocessing.

Model	$\rho_c [10^9 \text{ g cm}^{-3}]$	$X(^{16}\text{O})$	$X(^{12}\text{C})$	$X(^{22}\text{Ne})$	$Z [Z_\odot]$	$M(^{56}\text{Ni}) [M_\odot]$
1_1_1	1.0	0.7	0.2875	0.0125	0.5	0.2982
1_1_2	1.0	0.7	0.275	0.025	1.0	0.2876
1_1_3	1.0	0.7	0.225	0.075	3.0	0.2450
1_2_1	1.0	0.54	0.4475	0.0125	0.5	0.2966
1_2_2	1.0	0.54	0.435	0.025	1.0	0.2860
1_2_3	1.0	0.54	0.385	0.075	3.0	0.2444
1_3_1	1.0	0.38	0.6075	0.0125	0.5	0.2907
1_3_2	1.0	0.38	0.595	0.025	1.0	0.2805
1_3_3	1.0	0.38	0.545	0.075	3.0	0.2403
2_1_1	2.6	0.7	0.2875	0.0125	0.5	0.3115
2_1_2	2.6	0.7	0.275	0.025	1.0	0.2999
2_1_3	2.6	0.7	0.225	0.075	3.0	0.2544
2_2_1	2.6	0.54	0.4475	0.0125	0.5	0.3163
2_2_2	2.6	0.54	0.435	0.025	1.0	0.3046
2_2_3	2.6	0.54	0.385	0.075	3.0	0.2592
2_3_1	2.6	0.38	0.6075	0.0125	0.5	0.3174
2_3_2	2.6	0.38	0.595	0.025	1.0	0.3065
2_3_3	2.6	0.38	0.545	0.075	3.0	0.2608

high central density case (cf. Table 3). In order to check whether an under-representation of NSE-material in tracer particles in the low density case was the origin, we recalculated these models with the number of tracers increased to 35^3 . The trend of decreasing ^{56}Ni production with higher carbon mass fraction was weaker, but still had the same direction. Since the variations are at the percent level, it is beyond the accuracy of our models to judge whether the trend is of a physical nature or an artifact of our simulation.

The result of the ^{56}Ni production in the explosion phase being largely independent of the carbon mass fraction supports the conjecture of Röpke & Hillebrandt (2004) that the peak luminosity of SNe Ia will be only marginally affected by the carbon-to-oxygen ratio of the progenitor WD star. This conjecture was only based on the cumulative production of all iron group elements and is now confirmed by the derivation of the exact amounts of ^{56}Ni via nucleosynthetic postprocessing.

6.3. Impact of the central density on the ^{56}Ni mass

For fixed C/O ratios of 0.81 and solar metallicities our models produce $0.286 M_\odot$ of ^{56}Ni for $\rho_c = 1.0 \times 10^9 \text{ g cm}^{-3}$ and $0.305 M_\odot$ of ^{56}Ni for $\rho_c = 2.6 \times 10^9 \text{ g cm}^{-3}$, i.e. from the lower to the higher central density the ^{56}Ni production increases

for 7%. These changes go along with the higher overall production of iron group nuclei at higher central densities (cf. Table 3). The reasons for this effect were discussed in Sect. 5.2.

Although somewhat larger than the changes found in the case of varying carbon mass fraction, the effect is still rather small. However, our study covers only part of the effects resulting from changing the central densities of the models. With a further increasing central density, electron captures will become important and the ^{56}Ni production is expected to decrease while the total mass of iron group elements should still increase. Unfortunately, in the current study this effect could not be consistently modeled, but it will be addressed in forthcoming work.

6.4. Impact of the metallicity on the ^{56}Ni mass

Timmes et al. (2003) proposed an analytic model for the effect of the progenitor's metallicity on the ^{56}Ni production in SN Ia explosions. Their reasoning is based on the assumptions that most of the ^{56}Ni is produced between the $0.2 M_\odot$ and the $0.8 M_\odot$ mass shells in NSE and that the Y_e is constant during burning in that region. This is motivated by one-dimensional models. Moreover, they take into account only the species with the highest mass fraction; in a first step ^{56}Ni and ^{58}Ni . Under these

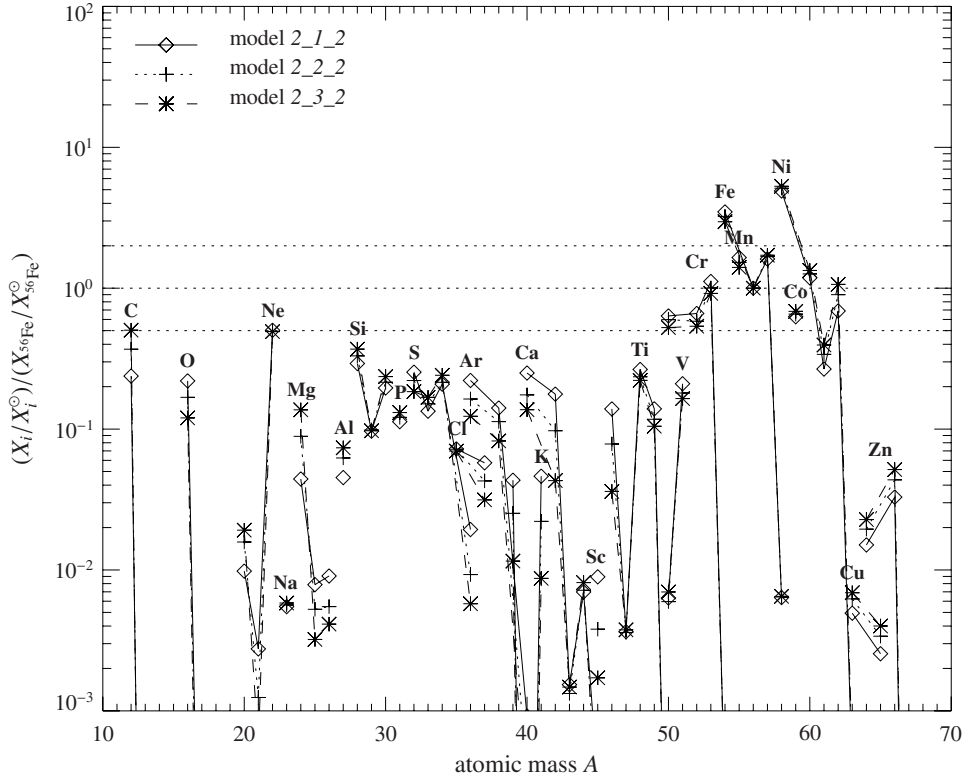


Fig. 11. Final abundances for models with different C/O ratios.

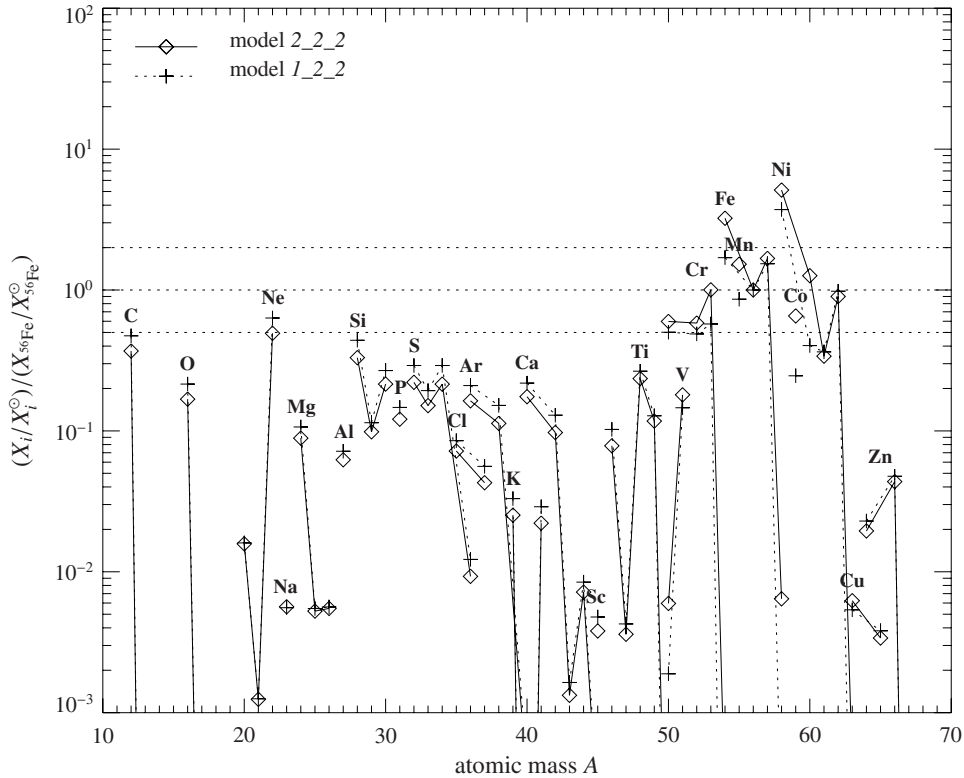


Fig. 12. Final abundances for models with different central densities.

assumptions they derive a linear correlation between Z and the produced $M(^{56}\text{Ni})$:

$$\frac{M_{56\text{Ni}}(\tilde{Z})}{M_{56\text{Ni}}(\tilde{Z} = 0)} = 1 - 0.057\tilde{Z},$$

with $\tilde{Z} = Z/Z_{\odot}$. This equation is obtained by combining the equations

$$(3) \quad \frac{M_{56\text{Ni}}}{M_{56\text{Ni}}(\tilde{Z} = 0)} = 58Y_e - 28, \quad (4)$$

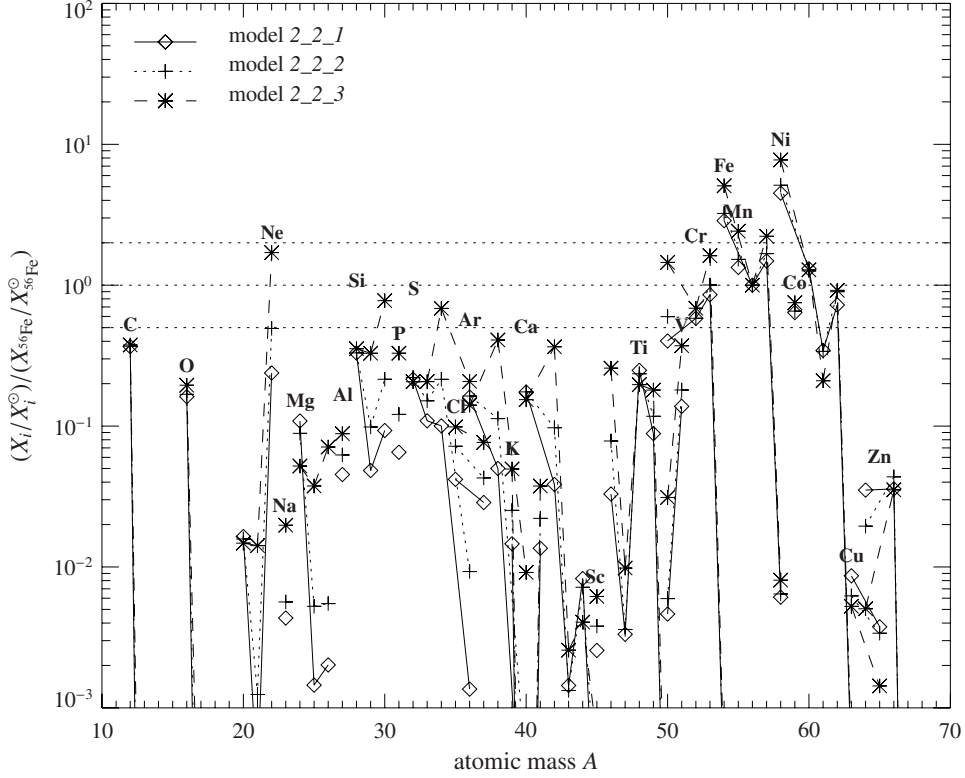


Fig. 13. Final abundances for models with different metallicities.

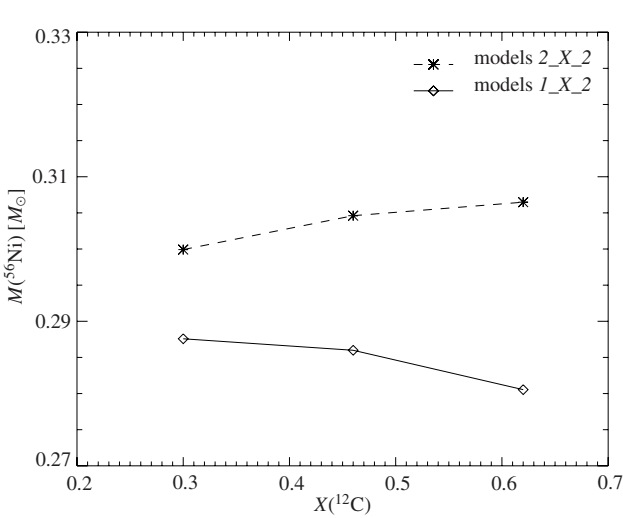


Fig. 14. ^{56}Ni production depending on the carbon mass fraction for models with different central densities and solar metallicity.

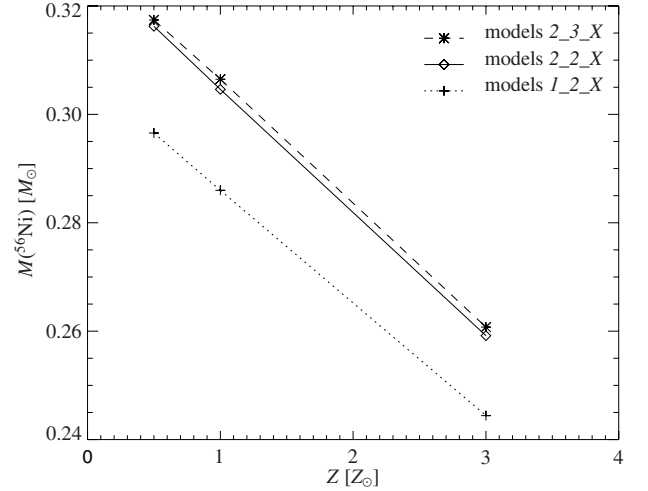


Fig. 15. ^{56}Ni production depending on the progenitor's metallicity for models with different central density and C/O ratio.

resulting from conservation of mass and charge,

$$X(^{22}\text{Ne}) = 22 \left(\frac{X(^{12}\text{C})}{12} + \frac{X(^{14}\text{N})}{14} + \frac{X(^{16}\text{O})}{16} \right), \quad (5)$$

approximating the ^{22}Ne abundance resulting from the metallicity of the ZAMS progenitor, and

$$Y_e = \frac{10}{22}X(^{22}\text{Ne}) + \frac{26}{56}X(^{56}\text{Fe}) + \frac{1}{2} [1 - X(^{22}\text{Ne}) - X(^{56}\text{Fe})],$$

giving the initial Y_e of the white dwarf just before the explosion under the assumption of a uniform distribution of ^{22}Ne and ^{56}Fe . When the presence of ^{54}Fe is taken into account the factor 0.057 in Eq. (3) changes to 0.054 (cf. Timmes et al. 2003).

For a comparison of this analytic prediction with our models we set $X(^{56}\text{Fe}) = 0$ in Eq. (6) since here the initial Y_e is determined by ^{22}Ne only. We set $X(^{22}\text{Ne}) = 0.025\tilde{Z}$. If Eq. (6) is now substituted into Eq. (4), the following equation is obtained

$$(6) \quad \frac{M_{56\text{Ni}}(\tilde{Z})}{M_{56\text{Ni}}(\tilde{Z} = 0)} = 1 - \frac{58}{22} 0.025\tilde{Z}. \quad (7)$$

Table 5. Fit parameters according to Eq. (8) from our models.

Model	1_1_X	1_2_X	1_3_X	2_1_X	2_2_X	2_3_X
$-m$	0.0213	0.0209	0.0201	0.0228	0.0228	0.0227
$M_0 [M_\odot]$	0.3089	0.3070	0.3007	0.3228	0.3275	0.3290
$-m/M_0 [M_\odot^{-1}]$	0.0690	0.0681	0.0668	0.0706	0.0696	0.0690

To compare this linear dependence of the ^{56}Ni mass on \tilde{Z} with our simulations, a linear regression following

$$M_{^{56}\text{Ni}}(\tilde{Z}) = M_0 + m\tilde{Z} \quad (8)$$

was applied to our data. Here M_0 denotes the extrapolated value $M(^{56}\text{Ni})$ at $\tilde{Z} = 0$. Values for m and M_0 for the different models are given in Table 5. The coefficient of correlation is 0.9999 in all cases, which suggests a good agreement of our data with a linear dependence, but, of course, more data points are needed for a definite statement.

To compare the slope of (7), i.e. -0.0659 , with the fits to our data, we give values for $-m/M_0$ in Table 5. The agreement is reasonable keeping in mind that Eqs. (3) and (7) were derived by assuming ^{56}Ni and ^{58}Ni to be the two most abundant isotopes in NSE with a constant Y_e . However, a significant amount of ^{56}Ni seems to be produced in regions where the assumption of constant Y_e breaks down.

Thus, the analytical model introduced in Timmes et al. (2003) provides an excellent explanation of the effect of the metallicity. Based on models different from the ones applied here, this was recently confirmed by Travaglio et al. (2005).

7. Conclusions

In the present paper the impact of several progenitor parameters on three-dimensional SN Ia explosion models has been studied for the first time in a systematic way. Here, we investigated the effects of the progenitor’s central density, its carbon mass fraction and its metallicity. Of course, there are several other parameters that may affect the light curve of SNe Ia (rotation of the progenitor, morphology of the ignition spot(s), a delayed detonation at varying densities, asphericities etc.), which were not addressed in the present survey.

Our numerical implementation as well as the underlying astrophysical model are robust against variations of the initial conditions to a reasonable degree. On the one hand, the variations in the resulting features are relatively small. A deviation in orders of magnitude would have been reason for concern, but all our models seem to be well-behaved. On the other hand, the model is not too robust in the sense that variations of the initial parameters do show effects on the results, i.e. an intrinsic variability is preserved. The degrees of freedom expected in SN Ia explosions are at least not entirely suppressed in our model. Hence our model fulfills the requirements 2, 3 and 4 stated by Hillebrandt & Niemeyer (2000).

Another point is the absolute scale of the results. Given the limited resources of computational time and storage space, we had to restrict the models to a resolution of $[256]^3$ grid cells per octant. Although such models reach numerical convergence in global characteristics (Reinecke et al. 2002c), it is not possible to apply multi-spot ignition scenarios at this resolution which would produce more vigorous explosions. As a consequence, the explosion energy of all our models is rather low and the ^{56}Ni production falls short of the nickel mass of a prototype SN Ia (Contardo et al. 2000, find $0.41 M_\odot$ of ^{56}Ni for SN1994D). As was recently shown (Blinnikov et al. 2006) synthetic light

curves for the models presented here nevertheless show reasonable agreement with observations of weaker SNe Ia.

These restrictions exclude the possibility of finding the absolute scale of effects and hence requirement 1 of Hillebrandt & Niemeyer (2000) is not met in the current study. However, there is a chance that models with more elaborate initial flame representations will agree better with the absolute values of observed quantities (see e.g. Travaglio et al. 2004)⁴. Nevertheless, the present parameter study should reveal the correct trends of the variation of SN Ia properties.

A major uncertainty lies in the range of variation of the progenitor parameters. Although we applied values that are common in the literature, our parameter space is not derived from a realistic stellar evolution of the progenitor.

Keeping this in mind, the maximum variation in ^{56}Ni of about 27% found in our parameter study can be regarded as a strong hint that the variations of the progenitor properties taken into account here provide a significant contribution to the scatter in SN Ia luminosities. However, it seems unlikely that these are sufficient to explain the full range of diversities in “Branch normal” SNe Ia. Of course, more elaborate models are required to assess this.

Regarding the diversity of ^{56}Ni production in our models resulting from the variation of the initial parameters, the following trends were found:

- The *progenitor’s carbon-to-oxygen ratio* has only little impact on the amount of produced ^{56}Ni . This is in strong contrast to the common assumption that the C/O ratio is a major source of luminosity variation in SN Ia explosions. The “working hypothesis” of Umeda et al. (1999a) could not be confirmed by our models. The reason for this effect was revealed by our three-dimensional simulations. Since flame propagation in the deflagration stage is mainly determined by the turbulent motions of the material, the explosion dynamics is not altered as long as the buoyancy effects that generate the turbulence are comparable. This is given in our models at stages of iron group nuclei synthesis. Different energy releases resulting from differences in the fuel binding energies are compensated by a varying amount of α -particles present in the ashes. These buffer the temperature of the ashes and thus the densities are not altered substantially, ensuring the same buoyancies. Consequently, the explosion dynamics is similar in the stages of iron group element synthesis for models with different C/O ratio in the fuel, resulting in a small variation of the produced ^{56}Ni of only about 2%. It is, however, not certain that the observed buffering effect suffices to compensate the energy release in NSE burning over a wider range of carbon mass fractions than studied here. Therefore, although we find little variation of the ^{56}Ni

⁴ For instance, Blinnikov et al. (2006) found good agreement between the synthetic light curves derived from the multi-spot ignition model *b_30_756* of Travaglio et al. (2004) and the observed light curves SN 1992A in the *B* and *V* bands. Whether the spectroscopic observations of SNe Ia can be reproduced by more elaborate deflagration models needs further study.

production with changing C/O ratio of the WD, this parameter cannot be completely ruled out as a source of SN Ia diversity. Our study suggests it plays only a secondary role in the deflagration models.

- The *central density* affects the ^{56}Ni production. The variation found in our models amounts to about 7%. This is explained by the fact that for higher central densities more material is burned under conditions where iron group elements are produced. Moreover, a higher central density increases the mean gravitational acceleration experienced by the flame front and thus enhances the generation of turbulence, thereby accelerating the flame propagation. Due to this effect even more material is processed at higher densities where the reactions terminate in iron group elements.
- A greater effect (assuming that our parameter space is reasonable) was found for a variation of the *metallicity* in the nuclear postprocessing. By varying the ^{22}Ne mass fraction from 0.5 to 3 times solar, a variation of the produced ^{56}Ni mass of about 20% was found. Our models were consistent with the analytical prediction of a linear relation between the metallicity and $X(^{56}\text{Ni})$ by Timmes et al. (2003).

The effects of varying C/O ratios and central densities of the progenitor on the supernova explosion are based on effects of the turbulent flame propagation and can thus only be revealed by three-dimensional models.

However, there is an important limitation to the results. Our analysis addresses only changes in the explosion process itself. For comparability of the simulations we assumed identical initial flame configurations. The ignition process, however, may be influenced by the carbon-to-oxygen ratio of the progenitor (Woosley et al. 2004). Since different initial flames can have a large impact on the explosion dynamics (e.g. Reinecke et al. 2002b; Gamezo et al. 2003; Calder et al. 2004; Röpke & Hillebrandt 2005a), the C/O ratio may still be an important parameter via this mechanism.

The present survey is incomplete towards higher densities, at which electron captures in the ashes become important. These shift the burning products to neutron-rich isotopes, favoring ^{58}Ni instead of ^{56}Ni . This effect would be taken into account in our postprocessing procedure, however electron captures may also become dynamically important with increasing central densities, since they reduce the electron pressure in the ashes. Unfortunately, this effect could not consistently be modeled in the current study. The explosion model assumes $Y_e = 0.5$. Effects of higher central densities will be addressed in forthcoming investigations.

7.1. Comparison with one-dimensional models

The effect of a variation in the carbon mass fraction of the progenitor on the produced ^{56}Ni mass was studied by Höflich et al. (1998). They applied a one-dimensional delayed detonation model. For a central density of $2.6 \times 10^9 \text{ g cm}^{-3}$, solar metallicity and a presumed deflagration-to-detonation transition at a density of $2.7 \times 10^7 \text{ g cm}^{-3}$ they calculated a model with a C/O ratio of 1/1 (DD21c in their notation) and a model with C/O reduced to 2/3. Here they find a decrease of the produced $M(^{56}\text{Ni})$ of about 14%. Assuming that a transition to detonation at such low densities as applied here does not alter the production of iron peak elements, a comparison with our models is possible. However, the results of Höflich et al. (1998) are in contrast with ours. This may be mainly due to the fact that the modeling of the correct implications of the C/O ratio on the explosion results

requires an accurate description of the multidimensional effects that dominate the flame propagation.

Bravo et al. (1993) investigated the impact of the ignition density on the ^{56}Ni production for one-dimensional deflagration models. For models with a central density of $2.5 \times 10^9 \text{ g cm}^{-3}$ (R2 in their notation) and $4.0 \times 10^9 \text{ g cm}^{-3}$ (R4) they find differences of about 7% which is in good agreement with our results.

Although our results regarding the change in ^{56}Ni production varying the metallicity are in good agreement with the analytical prediction by Timmes et al. (2003) and with the study by Travaglio et al. (2005), they disagree with the findings of Höflich et al. (1998), who report only a 5% effect on the ^{56}Ni production changing the metallicity from 0.1 Z_\odot to 10 Z_\odot . Contrary to this, the result of Iwamoto et al. (1999) that an increase of the metallicity from zero to solar decreases the ^{56}Ni production for about 8% is consistent with our results.

7.2. Cosmological significance

In order to discuss the cosmological significance of our results, we adopt a very simplistic view of the mechanism of the light curve. Following “Arnett’s rule” (Arnett 1982) we assume that the total mass of ^{56}Ni immediately determines the peak luminosity of the SN Ia event. Furthermore we assume that a larger energy released in the explosion leads to a more rapid decline of the light curve (Pinto & Eastman 2000). However, this may only have a second-order effect on the light-curve shape. The main parameter here is the opacity given by the distribution of heavy elements (Mazzali et al. 2001). This can only be adequately addressed in detailed synthetic light curve calculations and will be ignored here.

In the context of this simplification, none of the tested parameters reproduces the peak luminosity-light curve shape relation by lowering the produced ^{56}Ni mass accompanied by an increased energy release. While the carbon-to-oxygen ratio of the progenitor has little effect on the peak luminosity, it could alter the width of the light curve. The opposite holds for the progenitor’s metallicity. Here, the peak luminosity can vary by about 20%, but the explosion dynamics is unaffected. The central density prior to the ignition changes both the ^{56}Ni production and the energy release. Unfortunately our study is incomplete here. At higher values for the central density, the produced ^{56}Ni mass could decrease due to electron captures while the energy release may still increase. This has to be tested in further studies.

Another aspect is that we have ignored the interrelation of the parameters due to stellar evolution. This, however, predicts a lower C/O ratio for higher metallicities (cf. Umeda et al. 1999b). The effects of both parameters in this combination may reproduce the trend of the peak luminosity-light curve shape relation.

The final conclusions on the cosmological significance of the variations in the explosions found in the present study need to be drawn on the basis of synthetic light curves derived from our models. This is the subject of a subsequent publication.

Acknowledgements. This work was supported in part by the European Research Training Network “The Physics of type Ia Supernova Explosions” under contract HPRN-CT-2002-00303.

References

- Arnett, W. D. 1982, ApJ, 253, 785
 Barkat, Z., & Wheeler, J. C. 1990, ApJ, 355, 602
 Blinnikov, S. I., Röpke, F. K., Sorokina, E. I., et al. 2006, A&A, in press
 [arXiv:astro-ph/0603036]

- Brachwitz, F., Dean, D. J., Hix, W. R., et al. 2000, *ApJ*, 536, 934
- Bravo, E., Domínguez, I., Isern, J., et al. 1993, *A&A*, 269, 187
- Bravo, E., Tornambe, A., Domínguez, I., & Isern, J. 1996, *A&A*, 306, 811
- Calder, A. C., Plewa, T., Vladimirova, N., Lamb, D. Q., & Truran, J. W. 2004, [arXiv:astro-ph/0405126]
- Colella, P., & Woodward, P. R. 1984, *J. Comp. Phys.*, 54, 174
- Contardo, G., Leibundgut, B., & Vacca, W. D. 2000, *A&A*, 359, 876
- Damköhler, G. 1940, *Z. Elektroch.*, 46, 601
- Davies, R. M., & Taylor, G. 1950, *Proc. Roy. Soc. London A*, 200, 375
- Domínguez, I., & Höflich, P. 2000, *ApJ*, 528, 854
- Domínguez, I., Höflich, P., & Straniero, O. 2001, *ApJ*, 557, 279
- Domínguez, I., Höflich, P., Straniero, O., & Wheeler, C. 2000, *Mem. Soc. Astron. It.*, 71, 449
- Fryxell, B. A., Müller, E., & Arnett, W. D. 1989, Hydrodynamics and nuclear burning, MPA Green Report 449, Max-Planck-Institut für Astrophysik, Garching
- Gamezo, V. N., Khokhlov, A. M., & Oran, E. S. 2004, *Phys. Rev. Lett.*, 92, 211102
- Gamezo, V. N., Khokhlov, A. M., Oran, E. S., Chitchekanova, A. Y., & Rosenberg, R. O. 2003, *Science*, 299, 77
- Hernanz, M., Isern, J., Canal, R., Labay, J., & Mochkovitch, R. 1988, *ApJ*, 324, 331
- Hillebrandt, W., & Niemeyer, J. C. 2000, *ARA&A*, 38, 191
- Hillebrandt, W., Reinecke, M., & Niemeyer, J. C. 2000, in *Proc. of the XXXVth rencontres de Moriond: Energy densities in the universe*, ed. R. Anzari, Y. Giraud-Héraud, & J. Trân Thanh Vân (Thế Giới Publishers), 187
- Höflich, P., Wheeler, J. C., & Thielemann, F. K. 1998, *ApJ*, 495, 617
- Iwamoto, K., Brachwitz, F., Nomoto, K., et al. 1999, *ApJS*, 125, 439
- Khokhlov, A. M. 2000 [arXiv:astro-ph/0008463]
- Kozma, C., Fransson, C., Hillebrandt, W., et al. 2005, *A&A*, 437, 983
- Langanke, K., & Martínez-Pinedo, G. 2000, *Nucl. Phys. A*, 673, 481
- Langer, N., Deutschmann, A., Wellstein, S., & Höflich, P. 2000, *A&A*, 362, 1046
- Leibundgut, B. 2001, *ARA&A*, 39, 67
- Lesaffre, P., Podsiadlowski, P., & Tout, C. A. 2005, *MNRAS*, 356, 131
- Martínez-Pinedo, G., Langanke, K., & Dean, D. J. 2000, *ApJS*, 126, 493
- Mazzali, P. A., Nomoto, K., Cappellaro, E., et al. 2001, *ApJ*, 547, 988
- Mochkovitch, R. 1996, *A&A*, 311, 152
- Niemeyer, J. C. 1999, *ApJ*, 523, L57
- Niemeyer, J. C., & Hillebrandt, W. 1995, *ApJ*, 452, 769
- Nomoto, K., & Iben, I. 1985, *ApJ*, 297, 531
- Osher, S., & Sethian, J. A. 1988, *J. Comp. Phys.*, 79, 12
- Paczyński, B. 1972, *Astrophys. Lett.*, 11, 53
- Perlmutter, S., Aldering, G., Goldhaber, G., et al. 1999, *ApJ*, 517, 565
- Peters, N. 2000, *Turbulent Combustion* (Cambridge: Cambridge University Press)
- Phillips, M. M. 1993, *ApJ*, 413, L105
- Pinto, P. A., & Eastman, R. G. 2000, *ApJ*, 530, 744
- Reinecke, M., Hillebrandt, W., & Niemeyer, J. C. 1999a, *A&A*, 347, 739
- Reinecke, M., Hillebrandt, W., Niemeyer, J. C., Klein, R., & Gröbl, A. 1999b, *A&A*, 347, 724
- Reinecke, M. A. 2001, Ph.D. Thesis, Technical University of Munich, <http://www.ub.tum.de/medi en/emedi en.html>
- Reinecke, M., Hillebrandt, W., & Niemeyer, J. C. 2002a, *A&A*, 386, 936
- Reinecke, M., Hillebrandt, W., & Niemeyer, J. C. 2002b, *A&A*, 391, 1167
- Reinecke, M., Niemeyer, J. C., & Hillebrandt, W. 2002c, *New Astron. Rev.*, 46, 481
- Riess, A. G., Filippenko, A. V., Challis, P., et al. 1998, *AJ*, 116, 1009
- Röpke, F. K. 2005, *A&A*, 432, 969
- Röpke, F. K., & Hillebrandt, W. 2004, *A&A*, 420, L1
- Röpke, F. K., & Hillebrandt, W. 2005a, *A&A*, 431, 635
- Röpke, F. K., & Hillebrandt, W. 2005b, *A&A*, 429, L29
- Röpke, F. K., Hillebrandt, W., & Niemeyer, J. C. 2004a, *A&A*, 420, 411
- Röpke, F. K., Hillebrandt, W., & Niemeyer, J. C. 2004b, *A&A*, 421, 783
- Röpke, F. K., Hillebrandt, W., Niemeyer, J. C., & Woosley, S. E. 2006, *A&A*, 448, 1
- Röpke, F. K., Niemeyer, J. C., & Hillebrandt, W. 2003, *ApJ*, 588, 952
- Schmidt, W., & Niemeyer, J. C. 2006, *A&A*, 446, 627
- Thielemann, F., Nomoto, K., & Hashimoto, M. 1996, *ApJ*, 460, 408
- Thielemann, F.-K., Argast, D., Brachwitz, F., et al. 2003, in *From Twilight to Highlight: The Physics of Supernovae*, 331
- Thielemann, F.-K., Nomoto, K., & Yokoi, K. 1986, *A&A*, 158, 17
- Timmes, F. X., & Swesty, F. D. 2000, *ApJS*, 126, 501
- Timmes, F. X., & Woosley, S. E. 1992, *ApJ*, 396
- Timmes, F. X., Brown, E. F., & Truran, J. W. 2003, *ApJ*, 590, L83
- Travaglio, C., Hillebrandt, W., Reinecke, M., & Thielemann, F.-K. 2004, *A&A*, 425, 1029
- Travaglio, C., Hillebrandt, W., & Reinecke, M. 2005, *A&A*, 443, 1007
- Umeda, H., Nomoto, K., Kobayashi, C., Hachisu, I., & Kato, M. 1999a, *ApJ*, 522, L43
- Umeda, H., Nomoto, K., Yamaoka, H., & Wanajo, S. 1999b, *ApJ*, 513, 861
- Woosley, S. E., Wunsch, S., & Kuhlen, M. 2004, *ApJ*, 607, 921

Online Material

Table 6. Synthesized mass (M_{\odot}) for different models as plotted in Figs. 11–13.

Species	Model					
	<u>2_1_2</u>	<u>2_2_2</u>	<u>2_3_2</u>	<u>1_2_2</u>	<u>2_2_1</u>	<u>2_2_3</u>
¹² C	1.9875E-01	3.1231E-01	4.2854E-01	3.5180E-01	3.2127E-01	2.7646E-01
¹³ C	4.0934E-10	1.5019E-10	5.2597E-11	1.0447E-10	4.0874E-11	1.5923E-09
¹⁵ N	6.6972E-11	6.3314E-11	1.2747E-10	5.3309E-11	2.3057E-10	1.1065E-09
¹⁶ O	5.8071E-01	4.5006E-01	3.2308E-01	5.0524E-01	4.4801E-01	4.5299E-01
¹⁷ O	3.8492E-09	1.6084E-09	7.9966E-10	1.3737E-09	4.2219E-10	1.6026E-08
¹⁸ O	1.6529E-10	1.8213E-10	1.3201E-10	1.6677E-10	1.2570E-10	4.3167E-10
¹⁹ F	1.1308E-10	4.8632E-11	1.9358E-11	4.1208E-11	9.5085E-12	4.3938E-10
²⁰ Ne	4.3781E-03	7.1415E-03	8.7143E-03	6.3617E-03	7.6873E-03	5.7854E-03
²¹ Ne	3.1305E-06	1.4348E-06	6.6327E-07	1.2694E-06	3.6188E-07	1.4177E-05
²² Ne	1.8029E-02	1.7916E-02	1.7980E-02	2.0192E-02	8.9582E-03	5.3749E-02
²³ Na	5.0496E-05	5.2638E-05	5.4596E-05	4.5513E-05	4.1890E-05	1.5990E-04
²⁴ Mg	6.2728E-03	1.2767E-02	1.9800E-02	1.3463E-02	1.6159E-02	6.4936E-03
²⁵ Mg	1.4661E-04	9.9366E-05	6.0991E-05	9.1044E-05	2.8369E-05	6.1613E-04
²⁶ Mg	1.9381E-04	1.1919E-04	8.9878E-05	1.0706E-04	4.5240E-05	1.3344E-03
²⁷ Al	7.2327E-04	1.0101E-03	1.1982E-03	1.0191E-03	7.5928E-04	1.2407E-03
²⁸ Si	5.2546E-02	6.0341E-02	6.7721E-02	7.0398E-02	6.2266E-02	5.5974E-02
²⁹ Si	9.1322E-04	9.4254E-04	9.3651E-04	9.6043E-04	4.7884E-04	2.7276E-03
³⁰ Si	1.2685E-03	1.4113E-03	1.5581E-03	1.5451E-03	6.3194E-04	4.4249E-03
³¹ P	2.5345E-04	2.7570E-04	3.0006E-04	2.9326E-04	1.5368E-04	6.4987E-04
³² S	2.7642E-02	2.4441E-02	2.0486E-02	2.8237E-02	2.4557E-02	1.9786E-02
³³ S	1.1883E-04	1.3593E-04	1.5201E-04	1.5252E-04	1.0148E-04	1.6145E-04
³⁴ S	1.0709E-03	1.1193E-03	1.2621E-03	1.3314E-03	5.4058E-04	3.0902E-03
³⁶ S	5.0047E-07	2.4312E-07	1.5159E-07	2.8158E-07	3.6821E-08	4.7111E-06
³⁵ Cl	5.0421E-05	5.0890E-05	4.9569E-05	5.2873E-05	3.0618E-05	6.0507E-05
³⁷ Cl	1.3557E-05	1.0231E-05	7.5430E-06	1.1730E-05	7.0770E-06	1.5845E-05
³⁶ Ar	4.7197E-03	3.5313E-03	2.6786E-03	3.9809E-03	3.5923E-03	2.6380E-03
³⁸ Ar	5.9756E-04	4.8536E-04	3.5572E-04	5.7181E-04	2.2226E-04	1.5216E-03
⁴⁰ Ar	6.3966E-09	2.3371E-09	1.2911E-09	2.6198E-09	2.6172E-10	5.5970E-08
³⁹ K	4.1443E-05	2.4448E-05	1.1254E-05	2.8140E-05	1.4635E-05	4.1644E-05
⁴⁰ K	1.5893E-08	1.1857E-08	8.8932E-09	1.2172E-08	3.5607E-09	1.5243E-08
⁴¹ K	3.3541E-06	1.6253E-06	6.4371E-07	1.8679E-06	1.0319E-06	2.3920E-06
⁴⁰ Ca	4.1245E-03	2.9254E-03	2.3081E-03	3.2055E-03	3.0169E-03	2.2343E-03
⁴² Ca	2.0467E-05	1.1405E-05	5.0761E-06	1.3292E-05	4.6711E-06	3.7149E-05
⁴³ Ca	3.7921E-08	3.3294E-08	3.7149E-08	3.6033E-08	3.7361E-08	5.5808E-08
⁴⁴ Ca	2.7296E-06	2.8433E-06	3.2414E-06	2.9370E-06	3.3912E-06	1.3942E-06
⁴⁶ Ca	1.1429E-11	3.9578E-12	1.7961E-12	4.6778E-12	3.6129E-13	6.5306E-11
⁴⁸ Ca	5.1102E-16	4.0742E-17	8.4593E-18	4.7231E-17	7.0210E-19	3.8800E-14
⁴⁵ Sc	9.5903E-08	4.1321E-08	1.8759E-08	4.5593E-08	2.8767E-08	5.8257E-08
⁴⁶ Ti	8.5527E-06	4.8903E-06	2.2655E-06	5.6091E-06	2.1275E-06	1.3952E-05
⁴⁷ Ti	2.0932E-07	2.0933E-07	2.1956E-07	2.1773E-07	2.0015E-07	4.9531E-07
⁴⁸ Ti	1.5686E-04	1.4112E-04	1.3379E-04	1.3985E-04	1.5444E-04	1.0256E-04
⁴⁹ Ti	6.2734E-06	5.3616E-06	4.8099E-06	5.1362E-06	4.1781E-06	7.1369E-06
⁵⁰ Ti	4.0498E-10	3.9554E-10	4.0308E-10	3.3934E-11	3.5590E-10	1.1353E-09
⁵⁰ V	1.6127E-09	1.5420E-09	1.8142E-09	4.2838E-10	1.2401E-09	6.9824E-09
⁵¹ V	2.1755E-05	1.8974E-05	1.7403E-05	1.3477E-05	1.5028E-05	3.3895E-05
⁵⁰ Cr	1.2996E-04	1.2398E-04	1.0947E-04	9.1295E-05	8.6254E-05	2.6088E-04
⁵² Cr	2.7097E-03	2.4212E-03	2.2432E-03	1.7785E-03	2.5029E-03	2.4744E-03
⁵³ Cr	5.2887E-04	4.8179E-04	4.4336E-04	2.4196E-04	4.2566E-04	6.7475E-04
⁵⁴ Cr	2.8910E-08	2.9013E-08	2.8687E-08	5.3360E-11	2.7851E-08	3.6635E-08
⁵⁵ Mn	6.0348E-03	5.6617E-03	5.2371E-03	2.8042E-03	5.1364E-03	7.7788E-03
⁵⁴ Fe	6.8344E-02	6.4350E-02	5.9272E-02	2.9665E-02	5.9137E-02	8.7595E-02
⁵⁶ Fe	3.2193E-01	3.2643E-01	3.2811E-01	2.8657E-01	3.3773E-01	2.8308E-01
⁵⁷ Fe	1.2662E-02	1.3360E-02	1.3723E-02	1.0757E-02	1.2245E-02	1.5385E-02

Table 6. continued.

Species	Model					
	2_1_2	2_2_2	2_3_2	1_2_2	2_2_1	2_2_3
⁵⁸ Fe	6.4899E-06	6.6366E-06	6.7433E-06	1.2656E-07	6.5205E-06	7.2146E-06
⁵⁹ Co	5.8039E-04	6.1402E-04	6.4570E-04	2.0260E-04	6.2006E-04	6.1134E-04
⁵⁸ Ni	6.6717E-02	7.0699E-02	7.3404E-02	4.5109E-02	6.4330E-02	9.2729E-02
⁶⁰ Ni	6.3865E-03	6.9060E-03	7.3461E-03	1.9357E-03	7.3971E-03	6.0938E-03
⁶¹ Ni	6.3095E-05	8.1359E-05	9.5324E-05	7.6708E-05	8.5555E-05	4.3643E-05
⁶² Ni	5.2705E-04	6.9753E-04	8.2941E-04	6.6740E-04	5.8056E-04	6.1748E-04
⁶⁴ Ni	3.4339E-11	3.8872E-11	4.2017E-11	5.6274E-14	3.7882E-11	4.3591E-11
⁶³ Cu	7.8178E-07	1.0014E-06	1.1137E-06	7.5785E-07	1.4388E-06	7.3209E-07
⁶⁵ Cu	1.8541E-07	2.5041E-07	2.9743E-07	2.4756E-07	2.8771E-07	9.1714E-08
⁶⁴ Zn	4.1170E-06	5.4031E-06	6.3524E-06	5.5728E-06	1.0068E-05	1.2144E-06
⁶⁶ Zn	5.3276E-06	7.1634E-06	8.5197E-06	6.8650E-06	6.0776E-06	5.0221E-06
⁶⁷ Zn	2.1888E-12	2.7503E-12	3.2022E-12	1.0714E-12	2.5332E-12	2.9738E-12
⁶⁸ Zn	2.4497E-09	3.4762E-09	4.2682E-09	2.9172E-09	2.4247E-09	6.0432E-09
⁷⁰ Zn	1.6091E-19	2.1266E-19	2.3458E-19	1.4498E-23	2.0416E-19	2.5513E-19

Table 7. Synthesized mass (M_{\odot}) of radioactive species in different models.

Species	Model					
	2_1_2	2_2_2	2_3_2	1_2_2	2_2_1	2_2_3
²² Na	5.2892E-08	9.2173E-08	1.0290E-07	8.0645E-08	9.9089E-08	4.1895E-08
²⁶ Al	1.3078E-06	1.1027E-06	8.0954E-07	1.0024E-06	4.7110E-07	2.8228E-06
³⁶ Cl	7.6022E-07	7.2749E-07	6.8645E-07	8.1239E-07	2.8832E-07	1.1296E-06
³⁹ Ar	4.3326E-09	2.6531E-09	1.7073E-09	2.5865E-09	5.3153E-10	1.3045E-08
⁴⁰ K	1.5893E-08	1.1857E-08	8.8932E-09	1.2172E-08	3.5607E-09	1.5243E-08
⁴¹ Ca	3.3488E-06	1.6224E-06	6.4171E-07	1.8647E-06	1.0311E-06	2.3714E-06
⁴⁴ Ti	2.7207E-06	2.8370E-06	3.2374E-06	2.9291E-06	3.3876E-06	1.3530E-06
⁴⁸ V	2.7174E-08	1.6707E-08	1.0033E-08	1.9273E-08	1.0073E-08	4.0923E-08
⁴⁹ V	6.0178E-08	5.0885E-08	5.9430E-08	3.3875E-08	3.0780E-08	2.8737E-07
⁵³ Mn	2.0549E-04	1.9908E-04	1.9552E-04	1.6387E-05	1.9147E-04	2.7557E-04
⁵⁵ Fe	2.0833E-03	2.0297E-03	1.9799E-03	2.1947E-04	1.9797E-03	2.3335E-03
⁵⁹ Fe	8.7600E-13	9.1399E-13	9.4831E-13	8.2378E-17	8.7169E-13	1.1308E-12
⁶⁰ Fe	4.7700E-15	5.2457E-15	5.5233E-15	1.2764E-19	4.9474E-15	6.8064E-15
⁵⁶ Co	1.0058E-04	9.8004E-05	9.3479E-05	4.5078E-05	9.2616E-05	1.2481E-04
⁵⁷ Co	1.0771E-03	1.0724E-03	1.0677E-03	1.1285E-04	1.0531E-03	1.1640E-03
⁶⁰ Co	2.5561E-10	2.7429E-10	2.8596E-10	1.8310E-13	2.6598E-10	3.1485E-10
⁵⁶ Ni	2.9992E-01	3.0461E-01	3.0648E-01	2.8599E-01	3.1625E-01	2.5917E-01
⁵⁷ Ni	1.1578E-02	1.2281E-02	1.2648E-02	1.0643E-02	1.1183E-02	1.4214E-02
⁵⁹ Ni	4.6795E-04	4.7814E-04	4.8911E-04	8.0744E-05	4.6775E-04	5.2852E-04
⁶⁰ Ni	5.1163E-03	5.2800E-03	5.4430E-03	2.3015E-04	5.2058E-03	5.6263E-03
⁶¹ Ni	2.8036E-06	2.9852E-06	3.1293E-06	2.4920E-08	2.9360E-06	3.2136E-06
⁶² Ni	5.3714E-06	5.7961E-06	6.1280E-06	8.1844E-09	5.6628E-06	6.4208E-06
⁶³ Ni	2.2585E-11	2.5002E-11	2.6783E-11	3.4056E-15	2.4055E-11	2.9699E-11